Geophysical Journal International

Geophys. J. Int. (2018) **214,** 185–199
Advance Access publication 2018 March 21
GJI Geodynamics and tectonics

doi: 10.1093/gji/ggy114

The 2017 July 20 M_w 6.6 Bodrum–Kos earthquake illuminates active faulting in the Gulf of Gökova, SW Turkey

Ezgi Karasözen,[1] Edwin Nissen,[2] Pınar Büyükakpınar,[3] Musavver Didem Cambaz,[4] Metin Kahraman,[5] Esra Kalkan Ertan,[3] Bizhan Abgarmi,[6] Eric Bergman,[7] Abdolreza Ghods[8] and Atilla Arda Özacar[6]

[1] *Department of Geophysics, Colorado School of Mines,* 1500 *Illinois St, Golden, CO 80401, USA. E-mail: ekarasoz@mymail.mines.edu*
[2] *School of Earth and Ocean Sciences, University of Victoria, Victoria, BC V8P 5C2, Canada*
[3] *Department of Geophysics, Kandilli Observatory and Earthquake Research Institute, Boğaziçi University, 34684 Çengelköy, İstanbul, Turkey*
[4] *Regional Earthquake Tsunami Monitoring Center, Kandilli Observatory and Earthquake Research Institute, Boğaziçi University, 34684 Çengelköy, İstanbul, Turkey*
[5] *Department of Earthquake Engineering, Kandilli Observatory and Earthquake Research Institute, Boğaziçi University, 34684 Çengelköy, İstanbul, Turkey*
[6] *Department of Geological Engineering, Middle East Technical University, 06800 Ankara, Turkey*
[7] *Global Seismological Services, Golden, CO 80401, USA*
[8] *Department of Earth Sciences, Institute for Advanced Studies in Basic Sciences, University of Zanjan, 45195-1159 Zanjan, Iran*

Accepted 2018 March 20. Received 2018 March 14; in original form 2018 February 7

SUMMARY

The 2017 July 20 Bodrum–Kos earthquake (M_w 6.6) is the largest instrumentally recorded earthquake in the Gökova graben, one of the primary physiographic features of SW Turkey. Using seismology and satellite geodesy, we investigate its source characteristics, aftershock distribution, relationship with earlier instrumental seismicity, and association with known surface faulting. We show that the earthquake ruptured a planar (non-listric) normal fault that dips gently (∼37°) northwards beneath the northern Gulf of Gökova coastline, initiating at a depth of ∼11 km and rupturing upwards and bilaterally. Aftershocks concentrate around (but not necessarily on) the western, eastern and downdip edges of the ∼25 km-long rupture plane, and have maximum focal depths of ∼15 km. The main shock surface trace bounds a bathymetric ridge east of Kos island, and may be one of the several faults imaged previously in this area using seismic profiling and multibeam sonar. The fault thus lies within the hangingwall of the lower-angle (∼20° N-dipping) South Datça fault, which it presumably cross-cuts at depth. Through calibrated relocations, we confirm that sequences of moderate (M_w 5–5.5) earthquakes in 1989, 2004 and 2005 occurred in the eastern and central Gulf of Gökova, many of them likely within the hangingwall of the S-dipping Gökova fault. Overall, our results indicate a switch from dominant S-dipping normal faulting in the eastern graben to dominant N-dipping faulting in the west, but we find no support for a proposed NE–SW-trending left-lateral fault in the central Gulf; most colocated focal mechanisms involve ∼E–W normal faulting. Finally, the Bodrum–Kos main shock adds to growing set of examples from across the Aegean region of large normal faulting earthquakes that cut the seismogenic layer as simple planar structures.

Key words: Satellite geodesy; Earthquake source observations; Seismicity and tectonics.

1 INTRODUCTION

The 2017 July 20 M_w ∼6.6 Bodrum–Kos earthquake in the Gulf of Gökova was the largest earthquake in southwestern Turkey in nearly a half century (Fig. 1). It caused heavy damage to Bodrum, where ∼70 people were injured, and to the Greek island of Kos, where the strongest intensities were recorded (United States Geological Survey, USGS) and where two people were killed. Tsunami waves were observed on Kara Ada (Black Island), with maximum run-up of ∼2.0 m; on Bodrum peninsula (up to ∼1.9 m); and on Kos Island (up to ∼1.5 m) (Heidarzadeh *et al.* 2017; Yalçıner *et al.* 2017). The earthquake also generated a productive aftershock sequence, including around two thousand magnitude > 2 events surrounding the main shock within a month (International Seismological Centre bulletin), a separate cluster of events ∼30 km to the NE (Heidarzadeh *et al.* 2017), and a band of events up to ∼500 km NNW of the epicentre that was presumably triggered by transient, dynamic stresses (Pollitz *et al.* 2017).

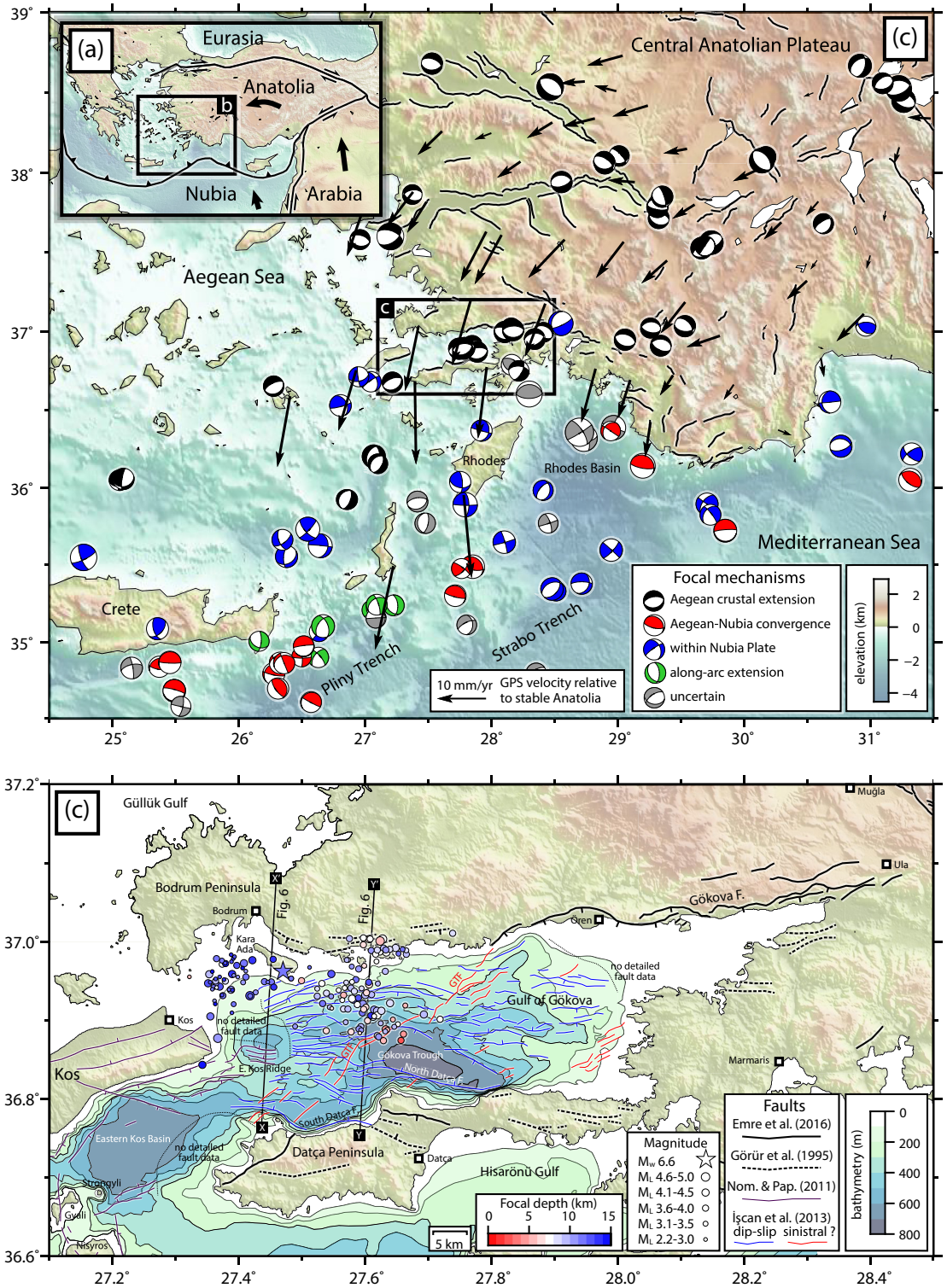

Figure 1. (a) Plate tectonic setting of the 2017 Bodrum–Kos earthquake. (b) Regional topography, earthquake focal mechanisms, GPS velocities and active faults. Focal mechanisms of $M_w \geq 5.0$ earthquakes spanning the period 1955–2014 are from the compilation by Howell *et al.* (2017). Following their scheme, we categorize mechanisms according to their tectonic significance: earthquakes associated with Aegean/Anatolian crustal extension are in black, those associated with Aegean-Nubian convergence are in red, those within subducting Nubian lithosphere are in blue, those associated with Hellenic arc-parallel crustal extension are in green and those of unknown association (mainly due to limited depth constraints) are in grey. GPS velocities are from Aktug *et al.* (2009), rotated into a stable Anatolia reference frame using their 'block 2' Euler pole, and active faults are from our own database. (c) Active faulting and bathymetry of the Gulf of Gökova with relocated hypocentral locations and depths of the 2017 Bodrum–Kos sequence. Onshore faults are from Görür *et al.* (1995) and Emre *et al.* (2016); offshore faults are from Nomikou & Papanikolaou (2011), İşcan *et al.* (2013) and Tur *et al.* (2015) (GTF = Gökova Transfer Fault). Bathymetric contours were digitized from Pe-Piper *et al.* (2005), Uluğ *et al.* (2005), Nomikou & Papanikolaou (2011), Kızıldağ *et al.* (2012), İşcan *et al.* (2013) and Tur *et al.* (2015). X–X' and Y–Y' are the cross-section lines for Fig. 6.

GPS velocities indicate western Turkey and the Aegean Sea to be among the most rapidly deforming zones of continental rifting globally (Fig. 1). This extension is driven by rollback of oceanic lithosphere of the Nubian plate as it subducts northwards under the Hellenic Arc (Reilinger *et al.* 2006) and/or gravitational collapse of elevated continental crust of the Central Anatolian Plateau (Aktug *et al.* 2009), and is manifest in thinned continental crust (e.g. Vanacore *et al.* 2013), in several mostly ∼E–W-trending grabens including the Gulf of Gökova (e.g. Emre *et al.* 2016), and in shallow normal faulting earthquake focal mechanisms (e.g. Taymaz *et al.* 1991; Kiratzi & Louvari 2003).

Two contrasting mechanisms of upper crustal extension are commonly invoked. On the one hand, exposure of the Oligocene-Miocene Cycladic and Menderes metamorphic core complexes is associated with listric normal faults that appear to grade into subhorizontal detachments at the brittle–ductile transition (e.g. Gessner *et al.* 2001). On the other hand, focal mechanisms of large modern earthquakes support planar faults that cut through the seismogenic layer and that can accommodate extension through 'bookshelf faulting', in which the faults and fault-bound blocks rotate about horizontal axes through time (Jackson & White 1989; Braunmiller & Nabelek 1996). The relative importance of these two modes of continental extension is controversial, but has critical implications for fault rheology and mechanics, basin formation and evolution, and seismic hazard.

The Gulf of Gökova and its surroundings also exhibit a variety of other earthquake types, including intermediate-depth earthquakes within the subducting Nubian plate and thrust events along its interface with overriding Aegean lithosphere (McKenzie 1972; Benetatos *et al.* 2004; Shaw & Jackson 2010; Howell *et al.* 2017). The volcanoes of Kefalos (western Kos island), Gyali, Strongyli and Nysiros, immediately west of the Gulf of Gökova, are another potential source of deformation and seismicity within this area (Papadopoulos *et al.* 1998; Stiros 2000; Caliro *et al.* 2005; Nomikou *et al.* 2013).

The 2017 Bodrum–Kos main shock is the largest modern instrumental earthquake in the Gulf of Gökova and so represents an opportunity to reassess the regional tectonics. Its source mechanism is also significant for understanding the induced tsunami waves (Heidarzadeh *et al.* 2017), and its rupture directivity may also be important for mapping the dynamic stresses responsible for triggering remote aftershocks (Pollitz *et al.* 2017). However, a previous GPS-derived main shock fault model by Tiryakioğlu *et al.* (2018) is inconsistent with most catalogue focal mechanisms and depths, and available tsunami waveforms appear too sparse to provide much additional detail (Heidarzadeh *et al.* 2017). The main purpose of this paper is to establish a main shock location, mechanism and slip distribution that are consistent both with relocated near-field aftershocks (Section 3), with regional and teleseismic waveforms (Section 4) and with InSAR and GPS data (Section 5). A secondary goal is to use these results as the basis of a reassessment of earlier instrumental seismicity, active faulting and modes of crustal extension in the Gulf of Gökova (Section 6).

2 BACKGROUND: ACTIVE FAULTING AND SEISMICITY OF THE GULF OF GÖKOVA

Though there are several competing models for the Oligocene and Miocene tectonic history of the Gökova region (e.g. Görür *et al.* 1995; Kurt *et al.* 1999; Yilmaz *et al.* 2000; Seyitoğlu *et al.* 2004; Gürer *et al.* 2013; Tur *et al.* 2015), there is consensus that the contemporary, N–S directed opening of the Gulf had initiated by the Pliocene. Onshore, active extension is most clearly tangible along the northern margin of the Gulf, where an S-dipping normal fault—which we call the Gökova fault zone after Şaroğlu *et al.* (1992) and Emre *et al.* (2016)—can be traced between Ula in the east and just west of Ören (Fig. 1c). Fieldwork we undertook along the coastal road between Ula and Ören revealed steep limestone fault planes dipping 58°–76° S (Supporting Information Fig. S1), with slickensides indicating slip vector azimuths (defined as the horizontal component of hangingwall motion with respect to the footwall) of 175°–195°, or S5°E–S15°W. Görür *et al.* (1995) extend this fault zone as far west as Bodrum, but it appears much more discontinuous in the west than in the east. Onshore faulting on the Datça peninsula, on the southern margin of the basin, is similarly discontinuous.

Offshore, single- and multichannel seismic reflection profiles and multibeam bathymetric surveying reveal numerous faults within the Gökova Basin (Kurt *et al.* 1999; Uluğ *et al.* 2005; Nomikou & Papanikolaou 2011; İşcan *et al.* 2013; Tur *et al.* 2015). In the east, several small ∼E–W-trending horst and graben structures presumably represent extension in the hangingwall of the Gökova fault zone. Water depths in the eastern Gulf are shallow and the thickness of the sedimentary basin fill is limited to at most a few hundred metres (Kurt *et al.* 1999).

In the central and western Gulf, N-dipping normal faulting just offshore the northern Datça peninsula—usually named collectively the Datça fault—appears dominant, responsible for the bathymetric low of the Gökova Trough, which also contains the thickest sedimentary basin fill within the entire graben, of ∼2.5 km (Kurt *et al.* 1999). In some maps, this faulting is divided into *en echelon*, left-stepping northern/eastern and southern/western segments (e.g. Uluğ *et al.* 2005), and from hereon we name these faults the North Datça fault and the South Datça fault. The North Datça fault is approximately planar in seismic images, but the South Datça fault appears listric, dipping ∼40° at the surface but only ∼20° at depths of ∼3 km, below which it ceases to be clearly imaged (Kurt *et al.* 1999). There are numerous N-dipping (synthetic) and S-dipping (antithetic) faults in the hangingwall of both faults. Kurt *et al.* (1999) and Uluğ *et al.* (2005) suggest that the S. Datça fault inherits its shallow dip from thrust sheets of the Lycian nappes, which likely form the basement in this area (Rimmelé *et al.* 2003), and that it was most active in the late Miocene–Pliocene, decelerating into the Pleistocene. In contrast, Seyitoğlu *et al.* (2004) mark the S. Datça fault as part of a major breakaway detachment of the Menderes Massif, active in the late Oligocene to early Miocene.

Uluğ *et al.* (2005) used the broad-scale bathymetry of the central Gulf of Gökova to propose an NE–SW-oriented left-lateral strike-slip fault, termed the Gökova Transfer Fault (GTF), that supposedly cross-cuts the E-W normal faults. Investigating this proposed structure using higher resolution multibeam data, İşcan *et al.* (2013) mapped a discontinuous alignment of SE-facing scarps, which in places offsets bathymetric contours in a left-lateral sense. On the basis that sinistral motion along the GTF would imply an N–S-oriented maximum principal compressive stress (σ_1) axis, İşcan *et al.* (2013) reinterpreted some of the nearby E-W structures as thrust scarps or folds, and went on to argue for a switch in the tectonic regime of the Gulf of Gökova during the Quaternary from N–S extension to active N–S compression. However, the putative left-lateral offsets were challenged by Tur *et al.* (2015), who instead interpreted the longest GTF scarp as an arcuate normal fault.

Further to the west, the ∼200 m-high submarine East Kos Ridge appears bounded by normal faulting (Nomikou & Papanikolaou 2011; Nomikou *et al.* 2013). Kos island itself is also flanked by normal faults on both margins, though the asymmetric onshore topography and offshore bathymetry mark the southern (offshore) S-dipping fault as dominant. Van Hinsbergen & Boekhout (2009) mapped a mid-Miocene N-dipping detachment fault in eastern Kos island, likely coeval with but not directly connected to the Cycladic and Menderes metamorphic core complexes further to the north.

There is a long record of damaging earthquakes in the Gulf of Gökova including significant historical events in 1493 CE (maximum intensity VII on Kos Island) and in 1869 CE (maximum intensity VIII on Datça peninsula) (Ergin *et al.* 1967). Large early instrumental events include an $M_S \sim 6.5$ earthquake in 1933 April 23 near Kos Island and $M_S \sim 6.0$ and ∼6.5 earthquakes in 1941 May 23 and December 13 close to Muğla, but source mechanisms and depths are unavailable and we know of no reports of surface rupturing. M_w 6.6 and 5.3 earthquakes in the northern Rhodes Basin and Hisarönü Gulf in 1961 May 23 and 1987 June 19 may represent Nubia-Aegean shortening along the easternmost Helenic Arc, although their locations and depths are poorly constrained relative to modern seismicity (McKenzie 1972; Benetatos *et al.* 2004). Most recently, Yolsal-Çevikbilen *et al.* (2014) investigated three sequences of moderate-sized events (M_w 5.1–5.4) in the central and eastern Gulf of Gökova in 1989 April 27–28, 2004 August 3–4 and 2005 January 10–11. Using regional first motions and teleseismic waveform modelling, they obtained centroid depths of ∼8–14 km and ∼E to ∼ENE-trending, S-dipping nodal planes with dips in the range 32–50°. We further discuss these recent sequences in Section 6.

The 2017 July 20 Bodrum–Kos earthquake occurred at 22:31 UTC in the north-western Gulf of Gökova (01:31 on 21 July, local time). Most standardized regional and global seismic catalogues—including those of the Disaster and Emergency Management Authority of Turkey (AFAD), the Kandilli Observatory and Earthquake Research Institute (KOERI), the European-Mediterranean Seismological Centre (EMSC), the International Seismological Centre (ISC) and the USGS National Earthquake Information Center (NEIC)—place its epicentre close to the island of Kara Ada in the northwestern Gulf, with an overall spread of around ∼10 km in location. Available catalogue focal mechanisms (Table 1) indicate nearly pure normal faulting on moderate angle (∼45° ± 10°) N- or S-dipping nodal planes, with centroid depths of 5–12 km (the AFAD 'focal' depth is ∼19 km). A finite fault model derived from regional GPS displacements (Table 2) indicates S-dipping faulting, but with a significant strike-slip component, which is missing from the seismological solutions, as well as an unusually shallow (∼1 km) depth for the peak slip (Tiryakioğlu *et al.* 2018). Modelling tsunami waveforms recorded at tide gauges in Bodrum and Syros (in the central Aegean Sea), Heidarzadeh *et al.* (2017) estimated a fault length of ∼25 km and a width of ∼15 km, but could not distinguish the dip direction.

3 CALIBRATED EARTHQUAKE RELOCATIONS

We reassess the hypocentre distribution of the 2017 Bodrum–Kos sequence using a multiple-earthquake relocation technique that exploits the availability of near-source seismic data and yields absolute, calibrated locations. Our initial aim is to constrain the main shock hypocentre (latitude, longitude and depth) and to illuminate its slip extents using the early aftershock distribution. Our relocation method—*mloc* (Bergman & Solomon 1990; Walker *et al.* 2011)—exploits the hypocentroidal decomposition (HD) algorithm of Jordan & Sverdrup (1981) that specifically minimizes systematic bias and fully interprets the location uncertainty, usually to better than 5 km. This approach has been applied to a number of recent earthquake sequences (Ghods *et al.* 2012; Hayes *et al.* 2014; Nealy *et al.* 2017) and a thorough description of our current implementation can be found in Karasözen *et al.* (2016).

By adapting the HD algorithm, the location problem for a cluster of seismic sources can be treated as two separate inverse problems. The first step is a relative relocation that calculates 'cluster vectors', which describe the relative location of each individual event with respect to the geometric mean of the cluster, the 'hypocentroid'. The second step solves for the absolute location of the hypocentroid and thereafter updates the absolute coordinates of all events in the cluster. A key advantage of *mloc* is its ability to use separate arrival time data sets at each step: all available data at any epicentral distance can be utilized for relative locations, whereas to achieve calibrated (absolute) hypocentres, direct arrival phases *Pg* and *Sg* at distances of <1° are preferred. This decomposition minimizes the bias of unknown Earth structure since only the portion of the travel-time data that is least susceptible to the path-correlated errors is modelled. However, there is still the portion of theoretical travel times that needs to be adjusted for the hypocentroid calculation. In order to minimize the error, we rely on modelling shorter path lengths, which depend on the availability of close-in seismic data with a good azimuthal coverage in the source region. The hypocentroid is then stable to the variations in the local velocity structure and, by using hundreds of readings from multiple events with fixed relative locations, a stable crustal model can be obtained. In addition, near-source direct *Pg* and *Sg* phases can also provide strong depth constraints up to epicentral distances of several times the focal depth.

This study benefited from an excellent station distribution that provided ∼1500 arrival times within an epicentral distance of ∼80 km for the calculation of the hypocentroid (Fig. 2a) and ∼13 000 arrival times for the calculation of the cluster vectors. These include local, regional and teleseismic phases reported by AFAD, KOERI, ISC, USGS NEIC and the Institute of Geodynamics of the National Observatory of Athens (NOA-IG). The best fit to *Pg* and *Sg* arrival times at this short range was achieved for a two-layered crust with 5.7 and 3.2 km s^{-1} for the top 20 km (Table 3). For the second layer, the fit to *Pn* and *Sn* arrivals was determined by setting crustal thickness as 35 km and lower crustal velocities as 6.3 and 3.65 km s^{-1}. The cluster vectors were relocated with a composite of this custom local model over the global standard 1-D model *ak*135 (Kennett *et al.* 1995). This Moho depth is considerably deeper than estimates of 24–27 km determined from receiver functions recorded at nearby stations at Kos, Bodrum and Datça (Sodoudi *et al.* 2006; Tezel *et al.* 2010; Vanacore *et al.* 2013). However, our estimate is influenced largely by arrivals up to ∼8° from the hypocentroid, and so averages over more than just the local crust. When we tried a shallower 30 km Moho, there were strong (∼2–3 s) positive residuals to P_n and S_n arrival times, especially at distances up to ∼7°. Furthermore, changes to the crustal thickness contributed little to the location accuracy since only relative travel-time data were used at this distance range (>0.8°), whereas direct arriving travel-time data were used to determine the hypocentroid at shorter distances (<0.8°).

Table 1. Source parameters of the 2017 July 20 Bodrum–Kos main shock derived from seismology. *SV* is the azimuth of the slip vector describing motion of the hangingwall relative to the footwall, assuming that the N-dipping nodal plane represents the fault. USGS = United States Geological Survey; GCMT = Global Centroid Moment Tensor Catalogue; GEOFON = GFZ Helmholtz-Zentrum Potsdam GEOFON Program; KOERI = Kandilli Observatory and Earthquake Research Institute; AFAD = Disaster and Emergency Management Authority of Turkey.

Source	Data	*N-dipping nodal plane*				*S-dipping nodal plane*			Centroid depth	Seismic moment	M_w
		Strike	Dip	Rake	SV	Strike	Dip	Rake			
USGS	global *W*-phases	285°	39°	−73°	353°	84°	53°	−103°	12 km	11.1×10^{18} Nm	6.6
USGS	global body waves	280°	37°	−79°	356°	86°	54°	−98°	5 km	7.6×10^{18} Nm	6.5
USGS	regional waveforms	268°	43°	−100°	012°	101°	47°	−81°	8 km	9.8×10^{18} Nm	6.6
GCMT	global waveforms	275°	36°	−85°	359°	89°	54°	−94°	12 km	11.6×10^{18} Nm	6.6
GEOFON	global waveforms	270°	56°	−94°	007°	97°	34°	−84°	11 km	9.7×10^{18} Nm	6.6
KOERI	regional waveforms	286°	53°	−72°	348°	78°	41°	−112°	6 km	11.3×10^{18} Nm	6.6
AFAD	regional waveforms	286°	38°	−80°	003°	93°	53°	−98°	19 km[a]	9.4×10^{18} Nm	6.5
This study	teleseismic body waves	$279^{\circ}\ ^{+25^{\circ}}_{-20^{\circ}}$	$37^{\circ}\ ^{+4^{\circ}}_{-4^{\circ}}$	$-75^{\circ}\ ^{+15^{\circ}}_{-10^{\circ}}$	$350^{\circ}\ ^{+12^{\circ}}_{-8^{\circ}}$	$80^{\circ}\ ^{+15^{\circ}}_{-10^{\circ}}$	$54^{\circ}\ ^{+5^{\circ}}_{-2^{\circ}}$	$-101^{\circ}\ ^{+8^{\circ}}_{-12^{\circ}}$	$7\ ^{+3}_{-2}$ km	6.8×10^{18} Nm	6.5

[a]AFAD lists the focal depth (of the hypocentre), not the centroid depth.

Table 2. Source parameters of the 2017 July 20 Bodrum–Kos main shock derived from geodesy. For our uniform slip model, latitude and longitude refer to the centre point of the surface fault. For our variable slip model, slip refers to the peak slip, and length, top depth and bottom depth describe the 0.2 m slip contour, which encompasses ∼90 per cent of the total moment.

Source	Data	Strike	Dip	Rake	SV	Slip	Longitude	Latitude	Length	Top	Bottom	Moment	M_w
Tiryakioğlu *et al.* (2018) *variable slip*	GPS	105°	57°	−62°	151°	0.26 m	N/A	N/A	N/A	N/A	N/A	10.9×10^{18} Nm	6.6
This study, uniform slip	GPS, InSAR	274.9° ± 2.6°	36.5° ± 1.0°	−79.5° ± 3.1°	351.9° ± 1.2°	1.46 m ± 0.12 m	27.474° ± 700 m	36.855° ± 300 m	16.8 km ± 0.8 km	1.2 km ± 0.3 km	9.1 km ± 0.4 km	10.4×10^{18} Nm ± 0.4× 10^{18} Nm	6.6
This study, variable slip	GPS, InSAR	274.9°	36.5°	−79.5°	351.9°	1.8 m	N/A	N/A	30 km	0 km	10 km	11.1×10^{18} Nm	6.6

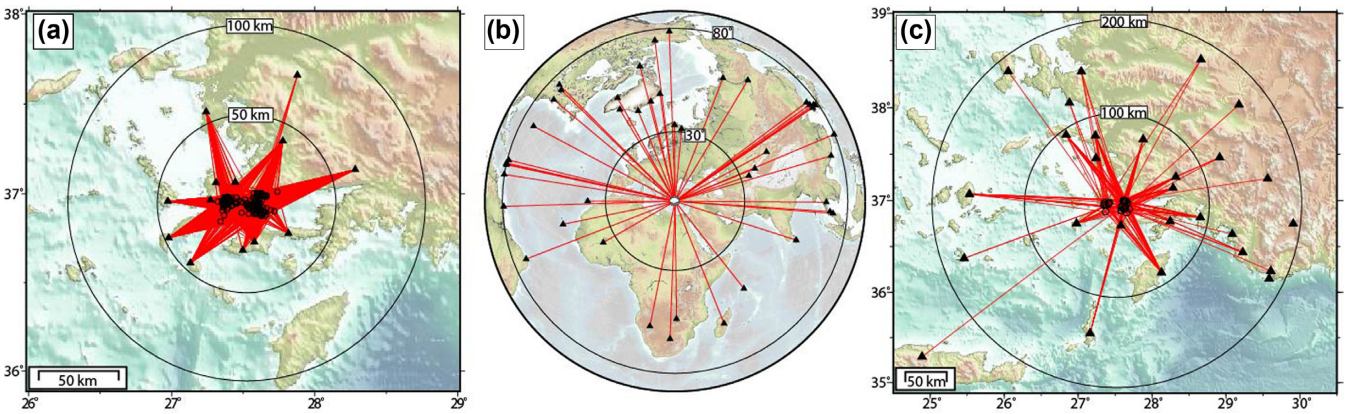

Figure 2. (a) Ray paths used in direct calibration of the hypocentroid (Section 3). Triangles denote seismic stations and black, open circles represent earthquakes. Black circles show radii of 50 and 100 km about the hypocentroid. (b) Stations used for modelling long-period teleseismic waveforms (Section 4.1). (b) Stations used for modelling regional waveforms (Section 4.2). Black circles show radii of 100 and 200 km about the centre of the cluster.

Table 3. The crustal model determined by and used in the earthquake relocation, as described in Section 3. The *ak*135 velocity model is used for all non-crustal phases for distances >17° (Kennett *et al.* 1995).

Depth to top of layer (km)	*P* velocity (km s^{-1})	*S* velocity (km s^{-1})
0	5.70	3.20
20	6.30	3.65
35	7.85	4.50

We relocated a cluster of 153 events including the Bodrum–Kos main shock, an $M_L \sim 2.6$ foreshock that preceded it by twenty-one minutes, and 151 aftershocks (Fig. 1c). Because the earliest aftershocks are likely to best illuminate the main shock fault plane (e.g. Henry & Das 2001), we only included the best-recorded early aftershocks within the western Gulf of Gökova. Nearly half of the aftershocks analysed occurred within one day of the main shock, three quarters within one week and all within a month. Absolute location uncertainties, which are given by the length of the larger semi-axes of the confidence ellipses (Supporting Information Table S1), are all <2 km. The favourable station distribution allowed depth to be treated as a free parameter for ∼70 per cent of the events in the cluster, with errors of <3 km (Supporting Information Table S1). Depths of remaining earthquakes were set manually by minimizing the residuals at nearby stations.

Our calibrated main shock hypocentre is located beneath the southern end of Kara Ada at a depth of ∼11 km, with its foreshock ∼1.5 km to the SE and at a similar depth (Fig. 1c). The aftershocks form two main groupings, one W and SW of the main shock between Kos and Kara Ada, and the other E of the main shock in the central Gulf. In map view, the early aftershock distribution therefore supports bilateral rupture of a ∼20–25 km-long, ∼W–E trending fault zone. However, their focal depths do not reveal a clear trend in either of the potential dip directions, implying that many lie off the main shock fault plane (we discuss this pattern in greater detail in Section 5). The western aftershocks mostly lie at depths of ∼9–14 km, while the eastern aftershocks concentrate within a broader but shallower depth range of ∼4–12 km.

The eastern seismicity includes a concentration of aftershocks along the coastline between Bodrum and Ören, close to the surface trace of several short, S-dipping normal faults mapped by Görür *et al.* (1995). In addition, several events at the easternmost extent of the aftershock distribution are in the vicinity of the proposed left-lateral Gökova Transfer Fault (Uluğ *et al.* 2005; İşcan *et al.* 2013). We return to these clusters of events in Sections 4.2, 5 and 6.

4 WAVEFORM MODELLING

4.1 Main shock: teleseismic body waves

We estimated the main shock source parameters and their uncertainties using the weighted least-squares algorithm of McCaffrey & Abers (1988) and McCaffrey *et al.* (1991) implemented within the MT5 program of Zwick *et al.* (1994). This is done by inverting long-period (15–100 s) *P* and *SH* waveforms recorded by Global Digital Seismic Network stations in the distance range 30°–80° (Fig. 2b). We selected 22 *P* and 26 *SH* seismograms that contained clear onset times in the broad-band records and that collectively provided an even azimuthal coverage. We solved for the strike, dip, rake, depth, source time function and moment of a point source by minimizing misfits between observed vertical (*P*) and transverse (*SH*) seismograms and synthesized *P*, *pP*, *sP*, *S* and *sS* waveforms (e.g. Nabelek 1984; Molnar & Lyon-Caen 1989; Taymaz *et al.* 1991; Emmerson *et al.* 2006). The synthetic seismograms were computed using a near-source upper crustal velocity model consistent with the one we obtained from calibrated earthquake relocations (Section 3); the shallow bathymetry of the northwestern Gulf of Gökova does not necessitate a water layer, and so we used half-space values of V_p 5.7 km s^{-1}, V_s 3.2 km s^{-1} and density 2700 kg m^{-3}. Once the minimum misfit solution was established, uncertainties were estimated by fixing individual parameters incrementally, solving for the best solution in each case, and determining the range of acceptable misfits by altering the parameters until a clear, visual degradation to the seismogram misfits could be detected.

Our minimum misfit solution (Fig. 3 and Table 1) is generally in good agreement with published catalogue solutions, with an ∼W–E-trending normal mechanism and moderate nodal plane dips of 37° $^{+4°}_{-4°}$N and 54° $^{+5°}_{-2°}$S. The centroid depth of 7 $^{+3}_{-2}$ km is consistent only with the shallower of the catalogue estimates: the USGS body-wave and regional moment tensor mechanisms and the KOERI solution.

On close inspection, many of the *SH* seismograms contain a late-arriving positive pulse—∼15 s after the *SH* first arrival at western azimuths (e.g. stations MACI, MPG) and ∼25 s afterwards at eastern azimuths (e.g. CHJ2, SRIT)—that is poorly fit by the synthetic waveforms. An equivalent feature may be present in some *P* seismograms, but it is harder to discern. Present across a range of azimuths, it probably results from complexity either in the earthquake source or in the surrounding velocity structure. To investigate further, we modelled the seismograms using two point sources, allowing both sets of source parameters as well as the relative timing and location to vary. Adding a second subevent neither reduces the overall numerical residuals nor improves the visual fit to this late pulse. This indicates that at the long periods sampled, the earthquake is best represented as a single point source.

We also tested explicitly for non-planar listric and antilistric fault geometries, imitated using three subevents ascribed a gradation of fixed depths and dips about the minimum-misfit single source values (Eyidoan & Jackson 1985; Braunmiller & Nabelek 1996; Karasözen *et al.* 2016; Reynolds & Copley 2018). Examining the N- and S-dipping nodal planes in turn, we kept strike and rake fixed at the single-source values and solved for the source time function of each subevent as well as their relative timing and location. Using a similar approach, Braunmiller & Nabelek (1996) and Reynolds & Copley (2018) showed that large anomalies in *SH* waveforms at azimuths within ±30° of the along-strike directions are most diagnostic of listric or antilistric normal faulting, and so we focused especially on the seismograms that fit this criterium. Imitating even minor (10°) listric or antilistric curvature worsens the misfit relative to the control case (three subevents of uniform 37° or 54° dip), both overall and at the subset of along-strike *SH* seismograms. To us, this is a strong indication that the Bodrum–Kos main shock involved planar faulting, and implies that complexities in near-source velocity structure are most likely responsible for some of the poor *SH* waveform misfits.

4.2 Aftershocks: regional waveform modelling

We determined source parameters of several of the largest aftershocks, with their uncertainties, by inverting regional waveforms using the ISOLA software package (Sokos & Zahradník 2008, 2013). This technique uses an iterative deconvolution inversion (Kikuchi & Kanamori 1991) to solve for the best single- or multiple-point source representation of the earthquake. Subevent moment tensors were estimated by a least-squares minimization of misfits between observed and synthetic waveforms; subevent positions and relative times were determined through grid search (Zahradník *et al.* 2005). In order to allow full wavefield representation at regional and local distances, Green's functions were calculated using the discrete wavenumber method of Bouchon (1981) and Coutant (1989).

We gathered waveform data recorded by stations of the Aristotle University of Thessaloniki (AUTH), AFAD, KOERI and NOA-IG networks over the distance range 50–250 km (Fig. 2c). The preferred frequency band for the inversion was selected after a careful analysis of the signal-to-noise ratio and station epicentral distances (Supporting Information Table S2), and Green's functions were estimated for the local velocity model obtained in Section 3 (Table 3). We initially determined mechanisms of 52 $M > 4$ aftershocks within a month of the main shock, using 3–14 stations for each event. However, mechanisms of many of the earliest aftershocks could not be resolved due to the contamination from the main shock coda, and we further eliminated regional moment tensors following the criteria of Sokos & Zahradník (2013), for a final total of 28 stable focal mechanisms (Fig. 4, Supporting Information Fig. S2, Supporting Information Table S2). Our results are also in good agreement with independent EMSC moment tensors, and by repeating the inversion

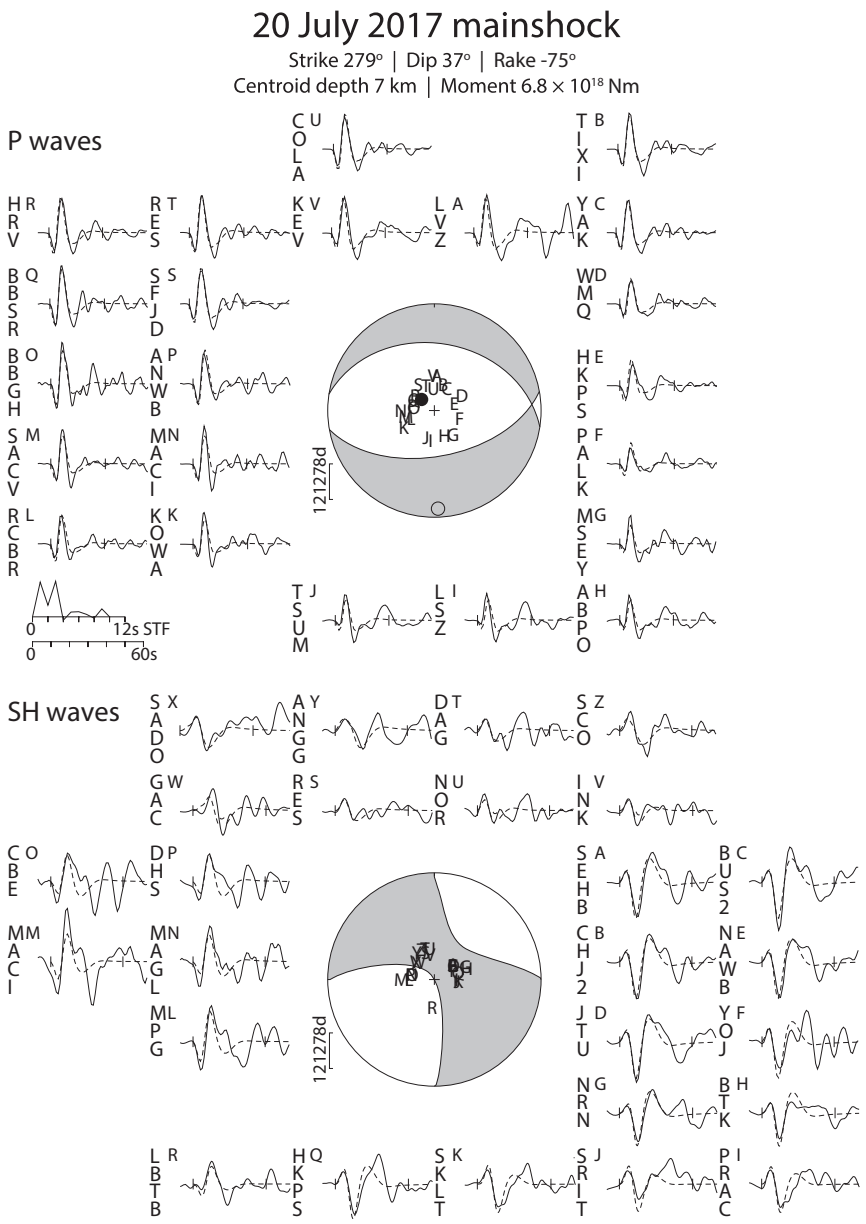

Figure 3. Minimum misfit solution for the 2017 July 20 Bodrum–Kos main shock from modelling teleseismic long-period body-waveforms. In the upper part, we plot the *P* focal sphere with nodal planes (lines), station positions (capital letters) and *P*- and *T*-axes (closed and open circles). Observed (solid) and synthetic (dashed) seismograms are plotted around the circumference, with the 30 s inversion window indicated by vertical ticks. Station codes are written vertically next to the focal sphere station position letter. In the lower part, we plot the *SH* focal sphere and seismograms; the inversion window is 40 s. The STF is the source–time function and the scale bar below it (in seconds) is that of the seismograms.

using an alternative regional velocity model (Akyol *et al.* 2006) and finding no large discrepancies, we are confident that our solutions are robust to realistic uncertainties in seismic structure (Supporting Information Table S3).

Aftershock centroid depths are between 3 and 14 km and are mostly shallower (typically by 1–6 km) than the hypocentre depths calculated in Section 3. This discrepancy is acceptable since only waveforms at regional distances are inverted in this study, resulting in uncertainties of several kilometres (>4 km) in centroid depth, compared to <3 km in focal depth (Supporting Information Table S1). Aftershock mechanisms exhibit a predominance of ∼E–W trending normal faulting, with nodal planes generally subparallel with those of the main shock. We see no evidence for subhorizontal nodal planes, as might be expected if the main shock faulting graded into a low-angle detachment at depth. In addition, aftershocks in close proximity to the proposed Gökova Transfer Fault (Uluğ *et al.* 2005; İşcan *et al.* 2013) show no indication of NE–SW left-lateral slip or N–S-oriented *P*-axes; most have ∼E–W-striking normal faulting mechanisms and thus ∼N–S-oriented *T*-axes.

5 INSAR AND GPS MODELLING

In this section, we model GPS and InSAR surface displacements to solve for the geometry and slip distribution of the Bodrum–Kos main shock faulting. GPS displacements are taken from Tiryakioğlu

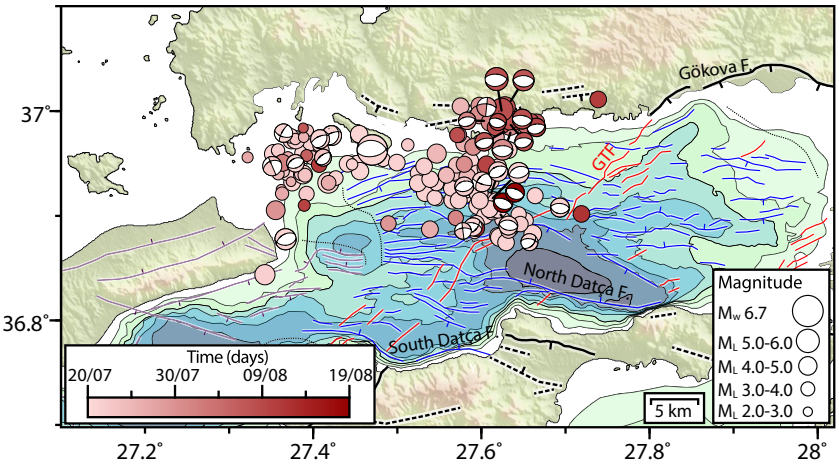

Figure 4. Focal mechanisms and calibrated earthquake locations of the 2017 Bodrum–Kos sequence coloured by date. All earthquakes are plotted at their relocated hypocentres (Section 3). The main shock mechanism is that determined from teleseismic body-waveform modelling (Section 4.1) and 28 aftershock mechanisms are determined from regional moment tensor inversion (Section 4.2). Source and hypocentre parameters of the regional moment tensor solutions are given in Supporting Information Table S2. Faults, topography and bathymetry are as in Fig. 1c.

et al. (2018) and comprise measurements from both continuous and campaign stations (Fig. 5a). Stations on Bodrum peninsula are observed to move northwards in the earthquake, with a peak horizontal displacement of ∼16 cm at Bodrum; a pair of stations on Datça peninsula move southwards by ∼5 and ∼3 cm. We constructed coseismic SAR interferograms using Sentinel-1 Interferometric Wideswath (IW) mode acquisitions on ascending track 131A and descending track 036D. For both imaging geometries, satellite line-of-sight vectors are inclined at ∼35° from the vertical at the earthquake epicentre. For the modelling, we used a single interferogram from each track, choosing the earliest possible post-event acquisition (2017 July 24 for both tracks) and pairing each with the pre-earthquake scene that minimizes the visible level of atmospheric noise (2017 July 12 on track 131A and 2017 June 30 on track 036D). At first glance, there is little obvious deformation across much of either interferogram (Figs 5a and b). At closer inspection, both interferograms exhibit six closely spaced E–W-trending fringes on Kara Ada—the consistency in pattern implying a signal dominated by subsidence—and, in the ascending interferogram, two fringes can also be observed at the far eastern end of Kos island.

Inverting only the GPS data for fault slip buried in an elastic half-space, Tiryakioğlu *et al.* (2018) deduced an S-dipping model fault (parameters in Table 2) whose surface trace lies ∼4 km south of Kara Ada, with two peaks in slip: one of 0.13 m centred at ∼8 km depth and ∼27.3° longitude, and the other of 0.26 m centred at ∼1 km depth and ∼27.5° longitude. We recognize various problems with Tiryakioğlu *et al.*'s model. First, it underpredicts horizontal displacements at the closest stations on Bodrum peninsula and fails to reproduce the observed southward motion of the closest station (KNID) on Datça peninsula. Second, their entire model fault plane lies south of both the relocated main shock hypocentre and the great majority of aftershocks. Thirdly, their ∼ESE-striking model fault is oblique to all of the surface faults mapped in the vicinity of its surface trace, which instead trend ∼ENE. Finally, their model strike (105°), rake (-62°) and peak slip depth (∼1 km) all lie well outside what we consider to be the acceptable bounds on nodal plane strike (70°–95°), rake (−103°––93°) and centroid depth (5–10 km), as determined by careful waveform modelling (Section 4 and Table 1).

Our own elastic dislocation modelling follows a standard protocol, described in detail elsewhere (e.g. Wright *et al.* 1999; Elliott *et al.* 2012). We first downsampled the InSAR data to concentrate sampling in areas with steep deformation gradients, and treated measurements on Kos and Kara Ada islands separately to those on the mainland to account for the ambiguity in relative displacement between each island and the mainland that arises during phase unwrapping. The InSAR data set was thereafter weighted equal to the GPS data set, for which only the horizontal components were used. We inverted first for uniform slip on a rectangular fault plane. Uncertainties in the uniform-slip source parameters were established through Monte Carlo inversions of 100 synthetic data sets perturbed with realistic noise; InSAR noise was characterized from undeformed parts of each interferogram and GPS noise was incorporated by picking at random from each station's 1σ error bounds (Tiryakioğlu *et al.* 2018). Once the geometry and rake were established, we solved for the pattern of slip on the fault.

We find that an S-dipping model fault can provide a good match to either the GPS data or the InSAR data, but not both. Furthermore, though the S-dipping model parameters are in better agreement with seismological values than those of Tiryakioğlu *et al.* (2018) are, the location of the model fault plane is still offset southwards from most of the relocated hypocentres (Supporting Information Fig. S2). The main shock hypocentre lies ∼11 km below the *surface trace* of the model fault, and is thus offset perpendicularly from the fault plane by ∼8 km, well above the errors in its hypocentre location and depth. On this basis, we rule out S-dipping faulting for the Bodrum–Kos main shock.

In contrast, an N-dipping model fault can match closely both the GPS and InSAR data—with root mean square errors of ∼5 mm for the GPS horizontal displacements and ∼3 mm for the InSAR line-of-sight displacements—while also agreeing well with constraints on fault location, geometry and depth from multi-event relocations and from body-waveform modelling (Figs 5c and d, Table 2). In contrast to the S-dipping case, the balance of weighting between the GPS and InSAR data makes little difference to the N-dipping fault plane parameters. The strike, dip and rake all lie within a few (at worst, six) degrees of our minimum-misfit waveform modelling values shown in Table 1. The fault dips gently ($36.5° \pm 1.0°$) northward beneath Kara Ada and the southern coastline of Bodrum peninsula, where InSAR data tightly constrain the downdip limit of

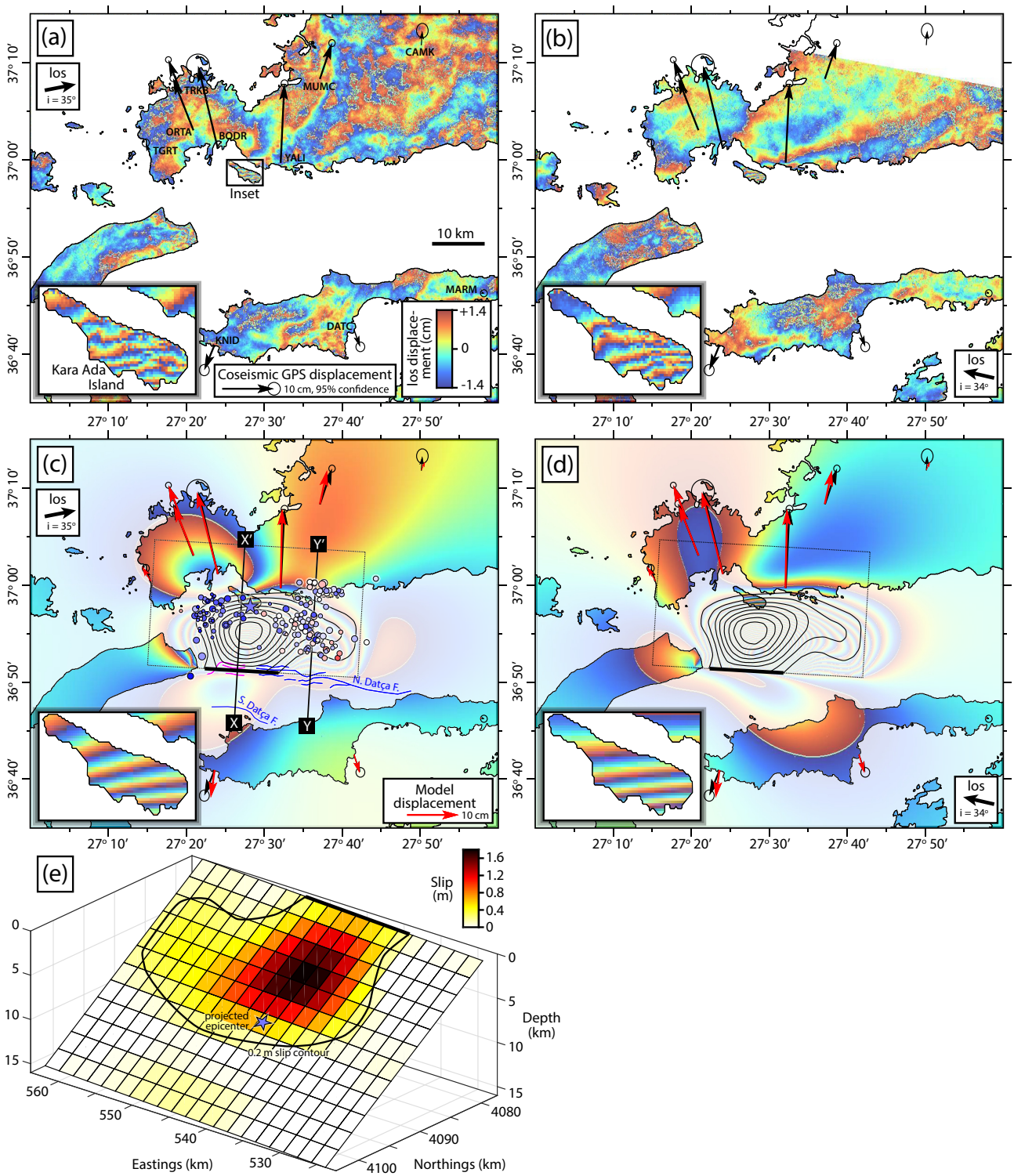

Figure 5. InSAR and GPS coseismic displacements and elastic dislocation model of the 2017 July 20 Bodrum–Kos main shock. (a) Ascending (2017 July 12–2017 July 24) and (b) descending (2017 June 30–2017 July 24) coseismic interferograms from Sentinel-1 tracks 131A and 036D, with observed GPS coseismic horizontal displacements with 95 per cent confidence ellipses from Tiryakioğlu *et al.* (2018). Insets show detailed view of Kara Ada island. (c) Ascending and (d) descending model interferograms and site displacements generated by the minimum-misfit elastic dislocation model shown in (e). In (c) and (d), the extended rectangular model fault plane shown in (e) is outlined by the dashed rectangle, slip contours at 0.2 m intervals are indicated by curved lines and the model surface rupture (with >0.2 m of slip) is in bold. In (e), only the 0.2 m slip contour is shown. In (c), we also plot relocated epicentres and key mapped surface faults, coloured and scaled as in Fig. 1c, as well as the cross-section lines X–X' and Y–Y' for Fig. 6.

slip. Similarly, InSAR measurements on Kos island dictate the western limit of faulting, but there is an absence of comparable near-field constraints on the eastern limit, which is consequently much more uncertain. The depth range of slip (0–10 km) is consistent with the

centroid depth of 7^{+3}_{-2} km and the fault length and width appear consistent with modelling of tsunami waveforms (Heidarzadeh *et al.* 2017). Peak slip of ∼1.8 m occurs at a depth of ∼4–5 km, though the distribution of slip on the shallowest part of the fault is poorly constrained due to the absence of near-field data, except perhaps in the far west beneath Kos Island (Fig. 5e).

The fault surface trace lies along the northern escarpment of East Kos Ridge, where it matches the location and strike of a parallel set of unnamed faults imaged both in multibeam bathymetry [see Nomikou & Papanikolaou (2011), fig. 1] and in shallow seismic profiles [see Uluğ *et al.* (2005), fig. 8; İşcan *et al.* (2013), figs 9 and 10; and Tur *et al.* (2015), fig. 9]. East Kos Ridge therefore comprises the uplifted footwall of the Bodrum–Kos main shock fault. At its eastern end, the main shock rupture lines up with the western end of the mapped, co-linear North Datça fault. We therefore propose that the 2017 Bodrum–Kos earthquake reveals an important western continuation of the North Datça fault that had not previously been fully recognized.

The main shock therefore lies within the hangingwall of the South Datça fault, which surfaces ∼7 km to the south. Imaged to depths of ∼3 km in multichannel seismic reflection lines, the South Datça fault is listric, inclined at ∼40° at the surface but dipping only ∼20° at depth (Kurt *et al.* 1999). We ran additional InSAR models to test explicitly for downdip curvature of the Bodrum–Kos main shock faulting; subfaults with imposed listric geometries produced a worse fit to the data than a planar fault, while depth-partitioned free dip solutions tended if anything towards slightly *antilistric* geometries, with minimal gains over the original and simpler planar case. Coupled with the equivalent tests undertaken during teleseismic waveform modelling (Section 4.1), this leads us to support simple planar faulting and rule out listricity. The steeper North Datça (Bodrum–Kos main shock) fault must therefore cross-cut the gentler South Datça fault, probably at a depth of around 4–5 km (Fig. 6). On the premise that through-going seismogenic faults cannot cross-cut one another, the South Datça fault is likely no longer a major active structure.

Our new geodetic model also motivates a reassessment of our earlier hypocentre relocations (Section 3). The main shock hypocentre beneath Kara Ada is located close to the downdip limit of fault slip and directly downdip from the peak slip (Figs 5c and e). The earthquake therefore ruptured upwards and bilaterally, which likely explains why the greatest damage occurred on eastern Kos Island, rather than on Bodrum peninsula, closer to the epicentre. In map view, aftershock epicentres appear to concentrate around the edges of the coseismic slip, with the caveat that the eastern limit of faulting is poorly constrained (Fig. 5c). However, viewed in cross section, it is evident that most aftershocks occur slightly below the main shock fault plane, rather than on it—even accounting for estimated uncertainties of ∼3 km in focal depth (Fig. 6). This relationship is consistent with several other recent main-shock–aftershock sequences from a variety of tectonic settings (Semmane *et al.* 2005; Roustaei *et al.* 2010; Nissen *et al.* 2014; Elliott *et al.* 2015; Wei *et al.* 2015; Karasözen *et al.* 2016).

5.1 Post-seismic deformation

In Section 3, we observe a conspicuous cluster of events at the northeastern edge of the aftershock zone. These started four days after the main shock in ∼2017 July 25 and culminated in the largest event of the (near field) aftershock sequence (ISC m_b 5.0; GCMT and USGS M_w 5.3) in 2017 August 8 (Fig. 4). Multi-event relocations confirm that these events lie outside of the main shock slip zone, as defined by the 0.2 m slip (90 per cent moment) contour, and that they group along an E–W trend that parallels the northern Gulf coastline (Figs 1c and 5c). Furthermore, in cross-section, the events appear to delineate a steep S-dipping plane approximately consistent with some of the short, S-dipping normal faults that Görür *et al.* (1995) mapped in this area (Fig. 6). Dip estimates for the S-dipping nodal plane of the largest 2017 August 8 aftershock are 37° (from Section 4.2), 49° (the USGS *W*-phase solution) and 41° (from the GCMT catalogue), and we obtain similar values for other aftershocks in this area. The faulting is therefore likely to be more moderately dipping than the steep trend in Fig. 6 implies.

Analysis of post-seismic InSAR imagery reveals a colocated and coeval zone of subsidence along this stretch of coastline (Figs 7c–e). From the size (1–2 fringes, or ∼3–6 cm in the satellite line-of-sight) and extent (∼10 km) of this signal, it is not clear whether the observed post-seismic deformation is due to the aftershock faulting, aseismic fault creep, viscoelastic relaxation or a combination of these processes. Simple forward models indicate the signal to be consistent either with slip on the S-dipping faults mapped by Görür *et al.* (1995) or with slip on the N-dipping main shock fault downdip of the principal slip patch.

6 DISCUSSION

The 2017 Bodrum–Kos sequence prompts us to reassess the tectonics of the broader Gulf of Gökova. To help this reinterpretation, we expanded our calibrated relocation analysis to include events from the past three decades (1987–2017) over the entire gulf. Early instrumental earthquakes can be successfully relocated together with recent events so long as they share several station readings (Walker *et al.* 2011; Karasözen *et al.* 2016). We included nine moderate M_w 5.1–5.4 earthquakes studied by Yolsal-Çevikbilen *et al.* (2014) and assigned centroid depths of 8–14 km and five other M_w 5.0–5.4 events with GCMT solutions; all have predominantly normal mechanisms. Also included in this broader cluster are four relatively far-field aftershocks of the Bodrum–Kos earthquake that occurred in 2017 August 13–14 in mountainous terrain ∼10 km north of the northern Gökova Gulf coastline.

We obtained 193 calibrated epicentres with errors less than 3 km (Fig. 8 and Supporting Information Table S4). We sat focal depths manually for recent events with available near and/or local arrival time data, and fixed the focal depth to 10 km for older events with no such data. Resulting focal depths lie between 5–16 km, in reasonable agreement with the range of 2–15 km observed in the 2017 Bodrum–Kos aftershock sequence (Section 3). Thus, the Bodrum–Kos main shock does not appear to have caused a temporary downwards expansion of the seismogenic zone, as has been observed following a few large Californian strike-slip earthquakes (Doser & Kanamori 1986; Schaff *et al.* 2002; Rolandone *et al.* 2004).

The decadal seismicity clusters in space and time into three main sequences prior to the 2017 Bodrum–Kos earthquake. The earliest sequence in 1989 includes two M_w 5.4 earthquakes and an M_w 5.1 event that we relocate to just north of the S-dipping Gökova fault trace (Fig. 8). These improved locations together with the available mechanisms (from Yolsal-Çevikbilen *et al.* (2014) and the GCMT catalogue) support rupture of smaller syn- or antithetic faults subparallel to but in the footwall of the Gökova fault. The S-dipping nodal planes of the centroid models are also more gently inclined (32°–33°) than surface exposures of the Gökova fault (58°–76°).

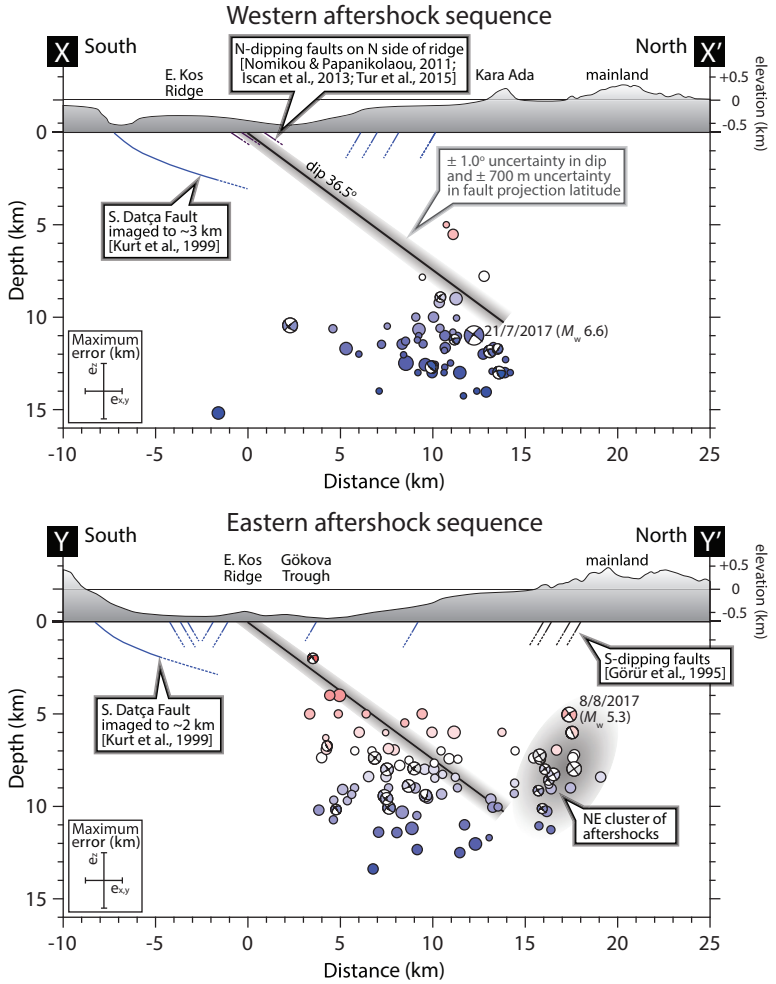

Figure 6. Cross-sections through relocated hypocentres of the 2017 Bodrum–Kos sequence, separated into (X–X', upper panel) those lying W of 27.5° longitude including the main shock, and (Y–Y', lower panel) those lying E of 27.5° longitude (see Fig. 1c for profile locations). Hypocentres and focal mechanisms are coloured and scaled as in Fig. 1(c). Maximum location error (e_z for depth, $e_{x,y}$ for latitude and longitude) for all events is shown in lower left corner in both panels; individual errors are given in Supporting Information Table S1. Simplified elevation profiles, constructed in part from the digitized bathymetric contours shown in Fig. 1c, are shown at the top of each panel with a vertical exaggeration of ×2.5. Distances along the *x*-axis are given relative to the surface trace of the InSAR/GPS-derived model fault plane, indicated by the black line; the profiles are constructed exactly perpendicular to this model fault. Key faults of interest are from Görür *et al.* (1995), Kurt *et al.* (1999), Nomikou & Papanikolaou (2011), İşcan *et al.* (2013) and Tur *et al.* (2015).

The second main sequence in August 2004 includes four M_w 5.1–5.4 earthquakes and the third in January 2005 includes a pair of M_w 5.2 earthquakes. The larger 2004–2005 events all have centroid depths of 8–13 km, gentle (34°–39°) S-dipping nodal planes and steeper (52°–56°) N-dipping nodal planes (Yolsal-Çevikbilen *et al.* 2014). The August 2004 earthquakes form a tight cluster in the north-central Gulf, ∼5–10 km S of the western end of the main Gökova fault, ∼10–15 km N of the N-dipping North Datça fault and just E of the Gökova Transfer Fault (Fig. 8). The January 2005 events lie immediately NE of the 2004 sequence and extend eastwards to the 1989 sequence. Available local-distance arrival-time data (*Pg* and *Sg* picks at 0.2–0.4°) support focal depths of 9–14 km depth, in very close agreement with the centroid estimates.

The dip directions of the 2004 and 2005 earthquakes are unclear. If they occurred on the Gökova fault, then it must be strongly listric. Alternatively, their locations and depths are approximately consistent with the base of the North Datça fault, particularly the August 2004 events, which align closely with the eastern edge of the 2017 aftershock sequence. However, considering the moderate moment magnitudes and likely source dimensions of <5 km, another possibility is that these earthquakes ruptured some of the many smaller N- and S-dipping faults imaged in bathymetric and seismic reflection data within the central Gökova Gulf (Kurt *et al.* 1999; Uluğ *et al.* 2005; İşcan *et al.* 2013; Tur *et al.* 2015). This is our preferred interpretation of these events, since it mimics faulting and seismicity patterns and magnitude relations observed in other continental rifts (e.g. Biggs *et al.* 2010).

Overall, the instrumental earthquake record and seismic imagery (Kurt *et al.* 1999) support a switch in the dip direction of the dominant normal faulting in the Gulf of Gökova, from S-dipping in the east (the Gökova fault) to N-dipping in the west (the North Datça fault, which cross-cuts an older N-dipping structure, the South Datça fault). The NE–SW alignment of scarps known as the Gökova Transfer Fault (Uluğ *et al.* 2005; İşcan *et al.* 2013) may play a role in the transition between these regimes, but we see no evidence of instrumental seismic activity along this trend. The easternmost 2017 Bodrum–Kos aftershocks and the western events of the August 2004

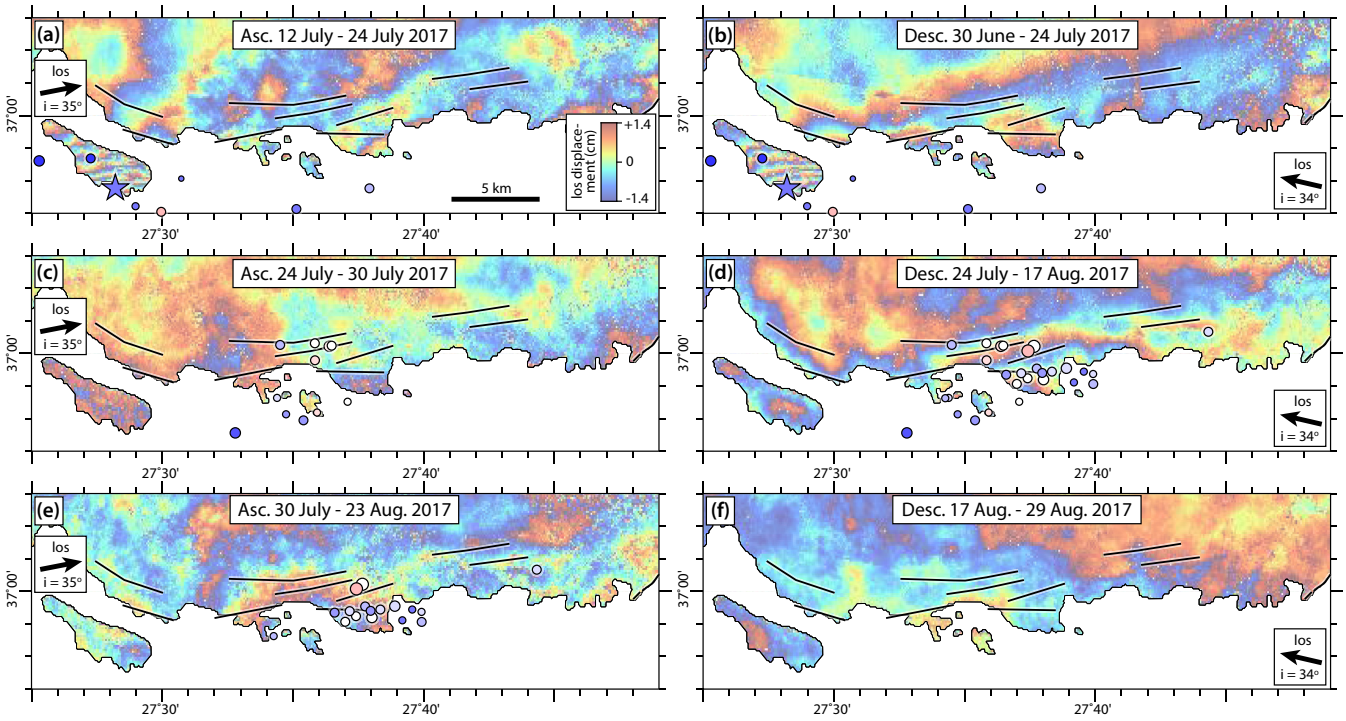

Figure 7. Coseismic and post-seismic interferograms in the area of a cluster of aftershocks that parallel the northern Gulf of Gökova coastline. Aftershocks are coloured and scaled as in Fig. 1c, and are further categorized by date according to the same timeframes as the interferograms. (a) and (b) show the same ascending and descending coseismic data as in Figs 5(c)–(d). (c) and (e) show post-seismic ascending interferograms, and (d) and (f) show post-seismic descending interferograms. Faults are from Görür *et al.* (1995).

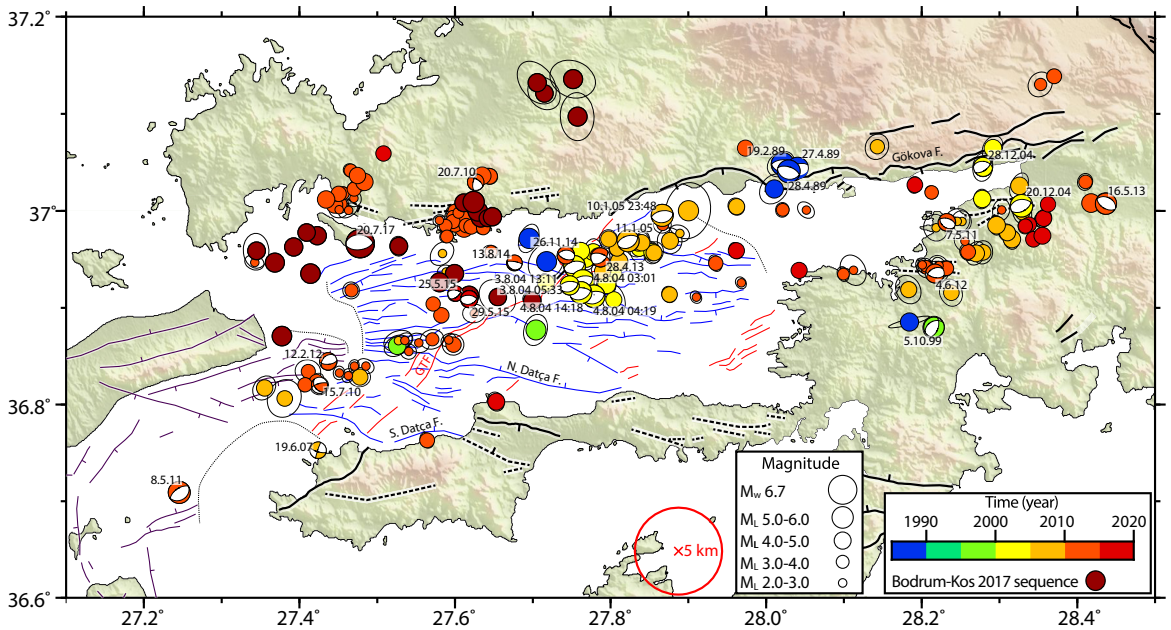

Figure 8. Relocated epicentres of earthquakes in the Gökova cluster with 90 per cent confidence ellipses that represent the absolute location error for each event. Available teleseismic focal mechanisms are taken from the AUTH, EMSC, GCMT, KOERI, NOA-IG and University of Athens catalogues, and from Benetatos *et al.* (2004) and Yolsal-Çevikbilen *et al.* (2014). Events are colour coded by time, with the 2017 Bodrum–Kos main-shock–aftershock sequence in dark red. Faulting is as in Fig. 1(c).

sequence are approximately colocated with the GTF, but most available focal mechanisms in this area—both before (Fig. 8) and after (Fig. 4) the 2017 Bodrum–Kos earthquake—indicate ~E–W normal faulting with ~N–S-oriented *T*-axes. A left-lateral GTF would imply ~N–S-oriented *P*-axes and so we agree with Tur *et al.*'s 2015 reinterpretation of the GTF as a zone of minor normal faults linking or cross-cutting the main E–W structures.

The switch in dominant dip direction is also apparent in the coastal geomorphology, which reflects the balance of local uplift and subsidence due to faulting and longer-wavelength vertical

motions such as from subduction processes or mantle convection (Howell *et al.* 2017). In general, subsiding hangingwalls of active normal faults give rise to drowned valleys and highly sinuous coastlines, whereas the uplifting footwalls produce straighter coastlines. Hence, east of ∼28° E, the southern Gulf of Gökova coastline is highly sinuous while the northern coastline is straight, reflecting the dominance of the S-dipping Gökova fault (Fig. 1c). West of ∼27.8°E, the northern Gulf coastline is more sinuous than the southern coastline, reflecting dominance of the North Datça fault (and before it, the South Datça fault). West of ∼27.35°E, there is a further switch to S-dipping faulting along the straight southern coastline of Kos island.

7 CONCLUSIONS

The 2017 M_w 6.6 Bodrum–Kos earthquake—the largest in southwestern Turkey in nearly 50 yr—prompts a reassessment of the tectonics of the Gökova graben. The association between this earthquake, earlier instrumental seismicity, and known surface faulting supports a switch from dominance of the S-dipping Gökova normal fault in the eastern graben to dominance of the N-dipping North Datça normal fault in the west. The 2017 Bodrum–Kos earthquake ruptured a westward continuation of the North Datça fault that dips ∼37° northwards and is responsible for uplifting a bathymetric ridge east of Kos island in its footwall. In explicitly ruling out listric geometries using independent teleseismic and geodetic data sets, we demonstrate that the earthquake cuts across the seismogenic layer as a simple, plaknar structure, bolstering similar findings for several other large continental normal faulting earthquakes both in the Greece–Turkey region (Braunmiller & Nabelek 1996; Karasözen *et al.* 2016) and globally (Reynolds & Copley 2018). The main shock fault plane lies in the hangingwall of the lower-angle (∼20° N-dipping) South Datça fault, which it cross-cuts at a depth of ∼4–5 km. Thus, although the South Datça fault dominated early opening of the western Gulf of Gökova and is still reflected in its bathymetry, it is no longer a through-going seismogenic structure. We suggest that only the Gökova and North Datça faults are capable of rupturing in large, M_w ∼ 6–7 earthquakes. Moderate magnitude (M_w ∼ 5–5.5) seismicity, such as the 2004–2005 earthquakes in the north-central Gulf, likely represents breaking up of the hangingwalls of these larger faults. Focal mechanisms in the vicinity of the proposed left-lateral Gökova Transfer Fault in the central Gulf support the reinterpretation of this feature as an alignment of minor normal fault scarps (Tur *et al.* 2015).

ACKNOWLEDGEMENTS

This work was supported by the National Science Foundation through Grant No. EAR 1524815, and grew out from an NSF-funded workshop in Middle East Technical University, Ankara, Turkey. EN acknowledges additional support from the Natural Sciences and Engineering Research Council of Canada (NSERC) through Discovery Grant No. 2017-04029, the Canada Foundation for Innovation (CFI), the British Columbia Knowledge Development Fund (BCKDF) and the Canada Research Chair program. We are grateful to Jochen Braunmiller and an anonymous reviewer for quick and thoughtful reviews of the manuscript. EN also thanks Bob Hilton for help during an earlier field trip to the Gökova region, made possible through a Roger Short Memorial Scholarship from University College, Oxford, and James Jackson for supporting a subsequent trip to the area. Phase arrival time data were gathered from the United States Geological Survey (USGS), the International Seismological Centre (ISC), the European-Mediterranean Seismological Centre (EMSC), the Kandilli Observatory and Earthquake Research Institute (KOERI) and the Disaster and Emergency Management Authority of Turkey (AFAD). Seismograms were downloaded from the Incorporated Research Institutions for Seismology (IRIS) Data Management Center. SAR interferograms were made using Copernicus Sentinel data [2017] with initial reconnaissance facilitated by use of the online LiCSAR database (Wright *et al.* 2016). Most of the figures were plotted using Generic Mapping Tools (Wessel *et al.* 2013).

REFERENCES

Aktug, B. *et al.*, 2009. Deformation of western Turkey from a combination of permanent and campaign GPS data: limits to block-like behavior, *J. geophys. Res.,* **114,** B10404, .

Akyol, N., Zhu, L., Mitchell, B.J., Sözbilir, H. & Kekovalı, K., 2006. Crustal structure and local seismicity in western Anatolia, *Geophys. J. Int.,* **166,** 1259–1269.

Benetatos, C., Kiratzi, A., Papazachos, C. & Karakaisis, G., 2004. Focal mechanisms of shallow and intermediate depth earthquakes along the Hellenic Arc, *J. Geodyn.,* **37,** 253–296.

Bergman, E.A. & Solomon, S.C., 1990. Earthquake swarms on the Mid-Atlantic Ridge—products of magmatism or extensional tectonics? *J. geophys. Res.,* **95,** 4943–4965.

Biggs, J., Nissen, E., Craig, T., Jackson, J. & Robinson, D.P., 2010. Breaking up the hanging wall of a rift-border fault: the 2009 Karonga earthquakes, Malawi, *Geophys. Res. Lett.,* **37,** L11305.

Bouchon, M., 1981. A simple method to calculate Green's functions for elastic layered media, *Bull. seism. Soc. Am.,* **71**(4), 959–971.

Braunmiller, J. & Nabelek, J., 1996. Geometry of continental normal faults: seismological constraints, *J. geophys. Res.,* **101,** 3045–3052.

Caliro, S., Chiodini, G., Galluzzo, D., Granieri, D., La Rocca, M., Saccorotti, G. & Ventura, G., 2005. Recent activity of Nisyros volcano (Greece) inferred from structural, geochemical and seismological data, *Bull. Volcanol.,* **67,** 358–369.

Coutant, O., 1989, *Program of numerical simulation AXITRA,* Tech. Rep, Université Joseph Fourier Grenoble, France.

Doser, D.I. & Kanamori, H., 1986. Depth of seismicity in the Imperial Valley Region (1977–1983) and its relationship to heat flow, crustal structure and the October 15, 1979, earthquake, *J. geophys. Res.,* **91,** 675–688.

Elliott, J.R., Nissen, E.K., England, P.C., Jackson, J.A., Lamb, S., Li, Z., Oehlers, M. & Parsons, B., 2012. Slip in the 2010–2011 Canterbury earthquakes, New Zealand, *J. geophys. Res.,* **117,** B03401.

Elliott, J.R. *et al.*, 2015. The 2013 M_w 6.2 Khaki-Shonbe (Iran) earthquake: insights into seismic and aseismic shortening of the Zagros sedimentary cover, *Earth Space Sci.,* **2**(11), 435–471.

Emmerson, B., Jackson, J., McKenzie, D. & Priestley, K., 2006. Seismicity, structure and rheology of the lithosphere in the Lake Baikal region, *Geophys. J. Int.,* **167,** 1233–1272.

Emre, Ö., Duman, T.Y., Özalp, S., Şaroğlu, F., Olgun, Ş., Elmacı, H. & Çan, T., 2016. Active fault database of Turkey, *Bull. Earthq. Eng.,* 1–47, doi.org/10.1007/s10518-016-0041-2.

Ergin, K., Güçlü, U. & Uz, Z., 1967. *Türkiye ve civarının deprem kataloğu, milâttan sonra 11 yılından 1964 sonuna kadar,* TC, İstanbul Teknik Üniversitesi, Maden Fakültesi, Arz Fiziği Enstitüsü.

Eyidoan, H. & Jackson, J., 1985. A seismological study of normal faulting in the Demirci, Alasehir and Gediz earthquakes of 1969–70 in western Turkey: implications for the nature and geometry of deformation in the continental crust, *Geophys. J. Int.,* **81,** 569–607.

Gessner, K., Ring, U., Johnson, C., Hetzel, R., Passchier, C.W. & Güngör, T., 2001. An active bivergent rolling-hinge detachment system: central Menderes metamorphic core complex in western Turkey, *Geology,* **29,** 611–614.

Ghods, A., Rezapour, M., Bergman, E., Mortezanejad, G. & Talebian, M., 2012. Relocation of the 2006 M_w 6.1 Silakhour, Iran, earthquake sequence: details of fault segmentation on the main recent fault, *Bull. seism. Soc. Am.,* **102,** 398–416.

Görür, N., Sengör, A.M.C., Sakinü, M., Akkök, R., Yiğitbaş, E. *et al.*, 1995. Rift formation in the Gökova region, southwest Anatolia: implications for the opening of the Aegean Sea, *Geol. Mag.,* **132**(6), 637–650.

Gürer, Ö.F., Sanğu, E., Özburan, M., Gürbüz, A. & Sarica-Filoreau, N., 2013. Complex basin evolution in the Gökova Gulf region: implications on the Late Cenozoic tectonics of southwest Turkey, *Int. J. Earth Sci.,* **102,** 2199–2221.

Hayes, G.P. *et al.*, 2014. Continuing megathrust earthquake potential in Chile after the 2014 Iquique earthquake, *Nature,* **512,** 295–298.

Heidarzadeh, M., Necmioglu, O., Ishibe, T. & Yalciner, A.C., 2017. Bodrum–Kos (Turkey-Greece) Mw 6.6 earthquake and tsunami of 20 July 2017: a test for the Mediterranean tsunami warning system, *Geosci. Lett.,* **4,** 31, doi:10.1186/s40562-017-0097-0.

Henry, C. & Das, S., 2001. Aftershock zones of large shallow earthquakes: fault dimensions, aftershock area expansion and scaling relations, *Geophys. J. Int.,* **147,** 272–293.

Howell, A., Jackson, J., Copley, A., McKenzie, D. & Nissen, E., 2017. Subduction and vertical coastal motions in the eastern Mediterranean, *Geophys. J. Int.,* **211,** 593–620.

İşcan, Y., Tur, H. & Gökaşan, E., 2013. Morphologic and seismic features of the Gulf of Gökova, SW Anatolia: evidence of strike-slip faulting with compression in the Aegean extensional regime, *Geo-Mar. Lett.,* **33,** 31–48.

Jackson, J.A. & White, N.J., 1989. Normal faulting in the upper continental crust: observations from regions of active extension, *J. Struct. Geol.,* **11,** 15–36.

Jordan, T.H. & Sverdrup, K.A., 1981. Teleseismic location techniques and their application to earthquake clusters in the South-Central Pacific, *Bull. seism. Soc. Am.,* **71,** 1105–1130.

Karasözen, E., Nissen, E., Bergman, E.A., Johnson, K.L. & Walters, R.J., 2016. Normal faulting in the Simav graben of western Turkey reassessed with calibrated earthquake relocations, *J. geophys. Res.,* **121,** 4553–4574.

Kennett, B.L.N., Engdahl, E.R. & Buland, R., 1995. Constraints on seismic velocities in the Earth from traveltimes, *Geophys. J. Int.,* **122,** 108–124.

Kikuchi, M. & Kanamori, H., 1991. Inversion of complex body waves—iii, *Bull. seism. Soc. Am.,* **81**(6), 2335–2350.

Kiratzi, A. & Louvari, E., 2003. Focal mechanisms of shallow earthquakes in the Aegean Sea and the surrounding lands determined by waveform modelling: a new database, *J. Geodyn.,* **36,** 251–274.

Kurt, H., Demirbağ, E. & Kuşçu, İ., 1999. Investigation of the submarine active tectonism in the Gulf of Gökova, southwest Anatolia southeast Aegean Sea, by multi-channel seismic reflection data, *Tectonophysics,* **305,** 477–496.

Kızıldağ, N., Özdas, A.H. & Uluğ, A., 2012. Late Pleistocene and Holocene sea level changes in the Hisarönü Gulf, southeast Aegean Sea, *Geoarchaeol. Int. J.,* **27**(3), 220–236.

McCaffrey, R. & Abers, G., 1988, SYN3: A Program for Inversion of Teleseismic Body Wave Forms on Microcomputers, *Air force geophysical laboratory technical report,* Hanscomb Air Force Base, Massachusetts.

McCaffrey, R., Zwick, P. & Abers, G., 1991, SYN4 Program, *Tech. rep.,* IASPEI Software Library.

McKenzie, D., 1972. Active Tectonics of the Mediterranean Region, *Geophys. J. Int.,* **30,** 109–185.

Molnar, P. & Lyon-Caen, H., 1989. Fault plane solutions of earthquakes and active tectonics of the Tibetan Plateau and its margins, *Geophys. J. Int.,* **99,** 123–154.

Nabelek, J.L., 1984, *Determination of earthquake source parameters from inversion of body waves, Ph.D. thesis*, M. I. T., Dept. of Earth, Atmospheric and Planetary Sciences, .

Nealy, J.L., Benz, H.M., Hayes, G.P., Bergman, E.A. & Barnhart, W.D., 2017. The 2008 Wells, Nevada, earthquake sequence: source constraints using calibrated multiple-event relocation and InSAR, *Bull. seism. Soc. Am.,* **107**(3), 1107–1117.

Nissen, E., Jackson, J., Jahani, S. & Tatar, M., 2014. Zagros "phantom earthquakes" reassessed—the interplay of seismicity and deep salt flow in the Simply Folded Belt? *J. geophys. Res.,* **119**(4), 3561–3583.

Nomikou, P. & Papanikolaou, D., 2011. Extension of active fault zones on Nisyros volcano across the Yali-Nisyros Channel based on onshore and offshore data, *Mar. Geophys. Res.,* **32,** 181–192.

Nomikou, P., Papanikolaou, D., Alexandri, M., Sakellariou, D. & Rousakis, G., 2013. Submarine volcanoes along the Aegean volcanic arc, *Tectonophysics,* **597,** 123–146.

Papadopoulos, G.A., Sachpazi, M., Panopoulou, G. & Stavrakakis, G., 1998. The volcanoseismic crisis of 1996-97 in Nisyros, SE Aegean Sea, Greece, *Terra Nova,* **10,** 151–154.

Pe-Piper, G., Piper, D.J.W. & Perissoratis, C., 2005. Neotectonics and the Kos Plateau Tuff eruption of 161 ka, South Aegean arc, *J. Volcanol. Geotherm. Res.,* **139,** 315–338.

Pollitz, F.F., Stein, R.S. & Sevilgen, V., 2017. Dynamic triggering of remote aftershocks of the M=6.6 July 20, 2017 Bodrum-Kos, Turkey, earthquake? in *AGU Fall Meeting Abstract.*

Reilinger, R., McClusky, S., Vernant, P., Lawrence, S., Ergintav, S., Cakmak, R., *et al.*, 2006 GPS constraints on continental deformation in the Africa–Arabia–Eurasia continental collision zone and implications for the dynamics of plate interactions *J. geophys. Res.,* **111,** B05411, doi:10.1029/2005JB004051.

Reynolds, K. & Copley, A., 2018. Seismological constraints on the down-dip shape of normal faults, *Geophys. J. Int.,* **213**(1), 534–560.

Rimmelé, G., Jolivet, L., Oberhänsli, R. & Goffé, B., 2003. Deformation history of the high-pressure Lycian Nappes and implications for tectonic evolution of SW Turkey, *Tectonics,* **22,** 1007, doi:10.1029/2001TC901041.

Rolandone, F., Bürgmann, R. & Nadeau, R.M., 2004. The evolution of the seismic-aseismic transition during the earthquake cycle: constraints from the time-dependent depth distribution of aftershocks, *Geophys. Res. Lett.,* **31,** doi:10.1029/2004GL021379.

Roustaei, M. *et al.*, 2010. The 25 March 2006 Fin earthquakes (Iran) – insights into the vertical extents of faulting in the Zagros Simply Folded Belt, *Geophys. J. Int.,* **181,** 1275–1291.

Şaroğlu, F., Emre, Ö. & Kuşçu, İ., 1992. *Active Fault Map of Turkey,* General Directorate of Mineral Research and Exploration.

Schaff, D.P., Bokelmann, G.H.R., Beroza, G.C., Waldhauser, F. & Ellsworth, W.L., 2002. High-resolution image of Calaveras Fault seismicity, *J. geophys. Res.,* **107,** 2186, doi:10.1029/2001JB000633.

Semmane, F., Cotton, F. & Campillo, M., 2005. The 2000 Tottori earthquake: a shallow earthquake with no surface rupture and slip properties controlled by depth, *J. geophys. Res.,* **110**(B9), B03306, doi:10.1029/2004JB003194.

Seyitoğlu, G., Içık, V. & Çemen, İ., 2004. Complete Tertiary exhumation history of the Menderes massif, western Turkey: an alternative working hypothesis, *Terra Nova,* **16,** 358–364.

Shaw, B. & Jackson, J., 2010. Earthquake mechanisms and active tectonics of the Hellenic subduction zone, *Geophys. J. Int.,* **181,** 966–984.

Sodoudi, F., *et al.*, 2006. Lithospheric structure of the Aegean obtained from P and S receiver functions, *J. geophys. Res.,* **111,** B12307, doi:10.1029/2005JB003932.

Sokos, E. & Zahradník, J., 2013. Evaluating centroid-moment-tensor uncertainty in the new version of isola software, *Seismol. Res. Lett.,* **84**(4), 656–665.

Sokos, E.N. & Zahradník, J., 2008. ISOLA a Fortran code and a Matlab GUI to perform multiple-point source inversion of seismic data, *Comput. Geosci.,* **34,** 967–977.

Stiros, S.C., 2000. Fault pattern of Nisyros Island volcano (Aegean Sea, Greece): structural, coastal and archaeological evidence, *Geol. Soc. London Spec. Publ.,* **171,** 385–397.

Taymaz, T., Jackson, J. & McKenzie, D., 1991. Active tectonics of the north and central Aegean Sea, *Geophys. J. Int.,* **106,** 433–490.

Tezel, T., Shibutani, T. & Kaypak, B., 2010. Crustal structure variation in western Turkey inferred from the receiver function analysis, *Tectonophysics,* **492,** 240–252.

Tiryakioğlu, İ. *et al.*, 2018. Slip distribution and source parameters of the 20 July 2017 Bodrum-Kos earthquake (M_w 6. 6) from GPS observations, *Geodinamica Acta,* **30**(1), 1–14.

Tur, H., Yaltırak, C., Elitez, İ. & Sarıkavak, K.T., 2015. Pliocene-Quaternary tectonic evolution of the Gulf of Gökova, southwest Turkey, *Tectonophysics,* **638,** 158–176.

Uluğ, A., Duman, M., Ersoy, Ş., Özel, E. & Avcı, M., 2005. Late Quaternary sea-level change, sedimentation and neotectonics of the Gulf of Gökova: Southeastern Aegean Sea, *Mar. Geol.,* **221**(1), 381–395.

Vanacore, E.A., Taymaz, T. & Saygin, E., 2013. Moho structure of the Anatolian Plate from receiver function analysis, *Geophys. J. Int.,* **193,** 329–337.

Van Hinsbergen, D.J.J. & Boekhout, F., 2009. Neogene brittle detachment faulting on Kos (E Greece): implications for a southern break-away fault of the Menderes metamorphic core complex (western Turkey), *Geol. Soc. London Spec. Publ.,* **311**(1), 311–320.

Walker, R.T., Bergman, E.A., Szeliga, W. & Fielding, E.J., 2011. Insights into the 1968-1997 Dasht-e-Bayaz and Zirkuh earthquake sequences, eastern Iran, from calibrated relocations, InSAR and high-resolution satellite imagery, *Geophys. J. Int.,* **187,** 1577–1603.

Wei, S., Barbot, S., Graves, R., Lienkaemper, J.J., Wang, T., Hudnut, K., Fu, Y. & Helmberger, D., 2015. The 2014 M_w 6.1 South Napa earthquake: A unilateral rupture with shallow asperity and rapid afterslip, *Seismol. Res. Lett.,* **86,** 344–354.

Wessel, P., Smith, W.H.F., Scharroo, R., Luis, J. & Wobbe, F., 2013. Generic Mapping Tools: Improved Version Released, *EOS, Trans. Am. Geophys. Un.,* **94,** 409–410.

Wright, T.J., Gonzalez, P.J., Walters, R.J., Hatton, E.L., Spaans, K. & Hooper, A.J., 2016. LiCSAR: Tools for automated generation of Sentinel-1 frame interferograms, in *AGU Fall Meeting Abstract.*

Wright, T.J., Parsons, B.E., Jackson, J.A., Haynes, M., Fielding, E.J., England, P.C. & Clarke, P.J., 1999. Source parameters of the 1 October 1995 Dinar (Turkey) earthquake from SAR interferometry and seismic body-wave modelling, *Earth planet. Sci. Lett.,* **172,** 23–37.

Yalçıner, A. *et al.*, 2017, *The 20th July 2017 (22:31 UTC) Bodrum-Kos Earthquake and Tsunami: Post Tsunami Field Survey Report,* Tech. Rep., Middle East Technical University.

Yilmaz, Y., Genc, S.C., Gurer, F., Bozcu, M., Yilmaz, K., Karacik, Z., Altunkaynak, S. & Elmas, A., 2000. When did the western Anatolian grabens begin to develop? *Geol. Soc. London Spec. Publ.,* **173,** 353–384.

Yolsal-Çevikbilen, S., Taymaz, T. & Helvacı, C., 2014. Earthquake mechanisms in the Gulfs of Gökova, Sığacık, Kuşadası, and the Simav Region (western Turkey): neotectonics, seismotectonics and geodynamic implications, *Tectonophysics,* **635,** 100–124.

Zahradník, J., Serpetsidaki, A., Sokos, E. & Tselentis, G.-A., 2005. Iterative deconvolution of regional waveforms and a double-event interpretation of the 2003 Lefkada earthquake, Greece, *Bull. seism. Soc. Am.,* **95**(1), 159–172.

Zwick, P., McCaffrey, R. & Abers, G., 1994. MT5 Program, *IASPEI Softw. Libr.,* **4**.

SUPPORTING INFORMATION

Supplementary data are available at *GJI* online.

Figure S1. Field photographs of the S-dipping Gökova fault.

Figure S2. An example regional moment tensor solution for the 2017 July 21 (03:59) M_w 4.2 event.

Figure S3. Uniform slip InSAR models.

Table S1. Calibrated earthquake relocations of the 2017 Bodrum–Kos sequence.

Table S2. Aftershock regional moment tensors using our preferred velocity model.

Table S3. Aftershock regional moment tensors using Akyol *et al.* (2006) velocities.

Table S4. Calibrated earthquake relocations of earlier Gökova seismicity.

Please note: Oxford University Press is not responsible for the content or functionality of any supporting materials supplied by the authors. Any queries (other than missing material) should be directed to the corresponding author for the paper.